Check for updates

Carrier doping modulates the magnetoelectronic and magnetic anisotropic properties of two-dimensional MSi$_2$N$_4$ (M = Cr, Mn, Fe, and Co) monolayers†

Ziyuan An,[a] Linhui Lv,[a] Ya Su,*[b] Yanyan Jiang[c] and Zhaoyong Guan ★[ad]

Through extensive density functional theory (DFT) calculations, our investigation delves into the stability, electrical characteristics, and magnetic behavior of monolayers (MLs) of MSi$_2$N$_4$. Computational analyses indicate intrinsic antiferromagnetic (AFM) orders within the MSi$_2$N$_4$ MLs, as a result of direct exchange interactions among transition metal (M) atoms. We further find that CrSi$_2$N$_4$ and CoSi$_2$N$_4$ MLs with primitive cells (pcells) exhibit half-metallic properties, with respective spin-β electron gaps of 3.661 and 2.021 eV. In contrast, MnSi$_2$N$_4$ and FeSi$_2$N$_4$ MLs with pcells act as semiconductors, having energy gaps of 0.427 and 0.282 eV, respectively. When the SOC is considered, the CrSi$_2$N$_4$, MnSi$_2$N$_4$ and FeSi$_2$N$_4$ MLs are metals, while the CoSi$_2$N$_4$ ML is a semiconductor. Our findings imply the dynamics and thermodynamic stability of MSi$_2$N$_4$ MLs. We have also explored the influence of carrier doping on the electromagnetic attributes of MSi$_2$N$_4$ MLs. Interestingly, charge doping could transform CrSi$_2$N$_4$, MnSi$_2$N$_4$, and CoSi$_2$N$_4$ MLs from their original AFM state into a ferromagnetic (FM) order. Moreover, carrier doping transformed CrSi$_2$N$_4$ and CoSi$_2$N$_4$ MLs from spin-polarized metals to half-metals (HMs). It is of particular note that doping of CrSi$_2$N$_4$ MLs with +0.9 e per pcell or more holes caused a switch in the easy axis (EA) to the [001] axis. The demonstrated intrinsic AFM order, excellent thermodynamic and kinetic stability, adjustable magnetism, and half-metallicity of the MSi$_2$N$_4$ family suggest its promising potential for applications in the realm of spintronics.

1. Introduction

Since the discovery of graphene,[1] the first two-dimensional (2D) material, through mechanical exfoliation, there has been great interest in 2D materials owing to their exemplary electrical,[2] thermal,[2] mechanical,[3,4] and chemical catalytic[5] properties. The potential of such materials is incredibly vast.[6–8] Nonetheless, the existence of long-range magnetic order at finite temperatures in these materials was considered unfeasible due

to thermal fluctuations as per the Mermin–Wagner theorem.[9] Initially, 2D FM materials had not been synthesized. The lack of 2D FM materials limits the application of 2D materials in spintronics and electronics. However, the synthesis of layered 2D FM CrI$_3$ has sparked new excitement in this field.[10] Following the discovery of CrI$_3$, the successful synthesis and characterization of other layered 2D FM materials[11–13] such as Fe$_3$GeTe$_2$,[14] Cr$_2$Ge$_2$Te$_6$,[15,16] and 2H-VSe$_2$[17] have been reported, and these materials are anticipated to invigorate the development of spintronics, data storage, magnetic electronic devices and magnetostrictive materials.[18–20] Hence, the research and development of 2D FM materials possess profound significance due to their promising potential applications.[21,22]

The layered MoSi$_2$N$_4$[23] ML has interesting properties.[24–29] The paramagnetic properties of this material,[30] however, limit its application in spintronics.[31,32] Encouragingly, there exist several common methods to investigate the magnetic ground states of 2D materials, including charge doping,[33] defect engineering,[34] stress engineering,[35] magnetic field manipulation,[36] intercalation,[37,38] and optical control.[39] Among these, charge doping is a practical and effective method[40] to modulate the electromagnetic properties of 2D materials,[41] and the utilization

[a] *Key Laboratory of Colloid and Interface Chemistry, Ministry of Education, School of Chemistry and Chemical Engineering, Shandong University, Jinan, Shandong 250100, P. R. China. E-mail: zyguan@sdu.edu.cn; Fax: +86-0531-88363179; Tel: +86-0531-88363179*

[b] *School of Electrical Engineering, Shandong University, Jinan, Shandong 250100, P. R. China. E-mail: suya@sdu.edu.cn; Fax: +86-0531-88392369; Tel: +86-0531-88392369*

[c] *Key Laboratory for Liquid–Solid Structural Evolution & Processing of Materials (Ministry of Education), School of Materials Science and Engineering, Shandong University, Jinan, Shandong, 250061, P. R. China*

[d] *School of Chemistry and Chemical Engineering, Shandong University, Jinan 250100, P. R. China*

† Electronic supplementary information (ESI) available. See DOI: https://doi.org/10.1039/d3cp05032g

of computational techniques may help alleviate the high experimental costs.

This paper studies MSi_2N_4 MLs due to their exceptional performance. Employing first-principles calculations based on DFT, we execute systematic research on MSi_2N_4. We investigate the geometry, electronic structures, stability, and magnetism of MSi_2N_4 MLs, and uncover the origin of the AFM ground state. Besides, $CrSi_2N_4$ and $CoSi_2N_4$ MLs with FM orders are HM. Charge doping enables the transition of magnetic order in $CrSi_2N_4$ and $MnSi_2N_4$. Additionally, charge doping prompts a switch in the EA of $CrSi_2N_4$ from [100] to [001] directions. Overall, this study propels the research trajectory of 2D magnetic materials, fostering their broad applications in the domain of spintronics.

2. Computational details

The geometries of MSi_2N_4 are searched by adopting the particle-swarm optimization (PSO) method with the CALPSO code and ASAP.[42] The plane-wave basis Vienna *ab initio* simulation package (VASP) code[43] is used to calculate MSi_2N_4 MLs. Perdew–Burke–Ernzerhof (PBE)[44] is adopted to deal with valence electrons. The range-separated hybrid Heyd–Scuseria–Ernzerhof (HSE06)[45,46] functional and GGA + U method[47] are applied to deal with the strong-correlated correction for the valence electrons, respectively. The effective onsite Coulomb interaction parameters (U) are set to 4.6 eV ($CrSi_2N_4$ and $MnSi_2N_4$), 6.0 eV ($FeSi_2N_4$), and 7.6 eV ($CoSi_2N_4$). The exchange interaction parameters (J_o) are set to 0.6 eV ($CrSi_2N_4$, $MnSi_2N_4$ and $CoSi_2N_4$) and 0.5 eV ($FeSi_2N_4$), respectively. Therefore, the effective $U_{eff}(U_{eff} = U - J_o)$ are set as 4.0 eV ($CrSi_2N_4$ and $MnSi_2N_4$), 5.5 eV ($FeSi_2N_4$), and 7.0 eV ($CoSi_2N_4$), and the corresponding references supporting these settings are shown in the ESI.[1] These U_{eff} are used in the calculation of the magnetic anisotropy energy (MAE), phonon spectra, and *ab initio* molecular dynamics (AIMD) simulation. Lattice constant c along the z-direction is set as 23 Å. The distance between adjacent interlayer atoms is 17 Å. The kinetic energy cutoff is set as 520 eV for all MSi_2N_4 MLs. The criteria of energy and force are 10^{-6} eV and 10 meV Å^{-1}, respectively. The geometry optimization and energy computation are performed by adopting $3 \times 3 \times 1$ and $9 \times 9 \times 1$ Monkhorst–Pack k-grids, respectively. The SOC is considered in calculation. After self-consistent calculations, total energies are evaluated by the noncollinear nonself-consistent calculations. The MAE is calculated with an energy cutoff of 600 eV, and the corresponding energy criterion is 1×10^{-8} eV. The corresponding $20 \times 20 \times 1$ k-grid is adopted with no symmetry constriction. Based on the finite displacement method, the phonon spectra and the phonon density of the states (PHDOS) are calculated using the Phonopy package.[48] To calculate phonon spectra and the PHDOS, a $4 \times 4 \times 1$ cell is adopted. The corresponding criterion of energy is set as 10^{-8} eV and the Hellmann–Feynman force is 1 meV Å^{-1}, respectively. 6000 uniform k-points along high-symmetry lines are adopted to get phonon spectra. AIMD simulation is also used to prove geometry stability. The
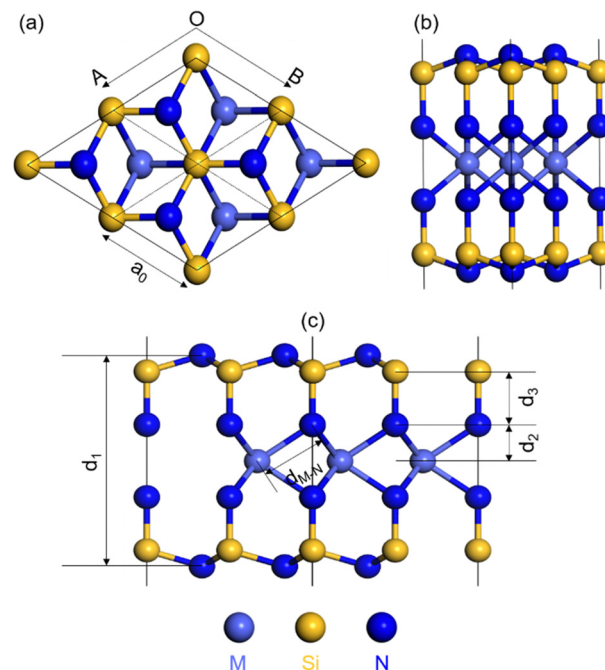

Fig. 1 Optimized geometries with (a) top and (b) and (c) side views of MSi_2N_4 MLs. The left, middle, and right balls at the bottom of (c) represent M, Si, and N atoms, respectively.

constant moles–volume–temperature ensemble with a Nosé–Hoover thermostat[49] is used at 300 K. The time step is 1 fs and the total time is 10 ps. To eliminate the effect of periodic boundary condition in a smaller system size, a $2 \times 2 \times 1$ cell (supercell) is adopted in AIMD simulation.

3. Results and discussion

3.1. Geometries of MSi_2N_4 MLs

The geometries of MSi_2N_4 ML have been computed and verified through the application of PSO[42] and ASAP methodologies, based on crystallographic structural analysis. Fig. S1 (ESI†) displays the optimal pcell configuration of the MSi_2N_4 MLs, whilst Fig. 1a–c shows the optimal geometries of the respective supercells. As indicated in Table 1, the determined lattice constants of MSi_2N_4 MLs are as follows: 2.909 Å for $CrSi_2N_4$, 2.920 Å for both $MnSi_2N_4$ and $FeSi_2N_4$, and 2.875 Å for $CoSi_2N_4$. Conversely, the $MoSi_2N_4$ ML exhibits a lattice constant of 2.910 Å. Atomic radius values of M are 118 pm (Cr), 117 pm (Mn), 117 pm (Fe), 116 pm (Co), and 130 pm (Mo), respectively.

This leads to comparable lattice parameters across the different MSi_2N_4 configurations. The interatomic distances

Table 1 Calculated lattice constants a_o, total energies E_t, and several interatomic distances for the AFM orders of MSi_2N_4

System	a_o (Å)	d_1 (Å)	d_2 (Å)	d_3 (Å)	d_{M-N} (Å)
$CrSi_2N_4$	2.909	6.879	1,174	1.750	2.049
$MnSi_2N_4$	2.920	6.858	1.170	1.745	2.052
$FeSi_2N_4$	2.920	6.858	1.170	1.745	2.052
$CoSi_2N_4$	2.875	6.989	1.199	1.762	2.048

This journal is © the Owner Societies 2024

Phys. Chem. Chem. Phys., 2024, **26**, 4208–4217 | **4209**
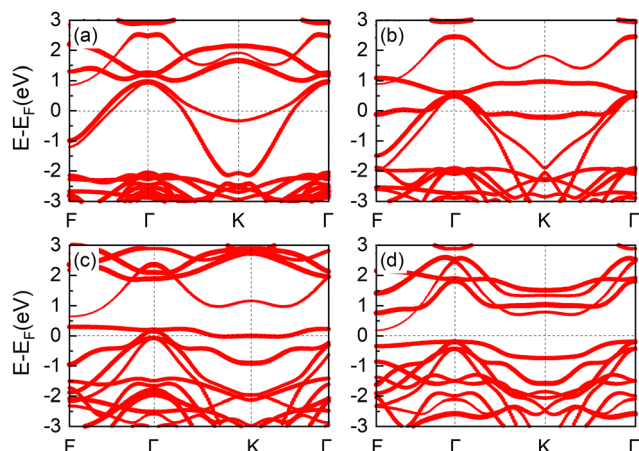
Fig. 2 Band structures of (a) CrSi$_2$N$_4$, (b) MnSi$_2$N$_4$, (c) FeSi$_2$N$_4$ and (d) CoSi$_2$N$_4$ MLs. The lines colored in red represent the electron channels.

Fig. 3 Spin charge densities of (a) AFM and (b) FM orders of CoSi$_2$N$_4$. The isovalues are 0.05 e Å^{-3} in (a) and 0.04 e Å^{-3} in (b), respectively. The red and blue colors represent spin-α and spin-β electrons, respectively. The spin-polarized band structures and PDOSs of (c) CrSi$_2$N$_4$, (d) MnSi$_2$N$_4$, (e) FeSi$_2$N$_4$, and (f) CoSi$_2$N$_4$ MLs, respectively. The solid and dashed lines represent spin-α and spin-β electrons, respectively.

between element M and nitrogen atoms have been calculated to be 2.049, 2.052, 2.052, and 2.048 Å, respectively.[50] These distances exhibit minor variation due to similarity in the atomic radii of the M elements. Further details pertaining to MSi$_2$N$_4$ can be seen in Table 1. The optimized geometries of the MSi$_2$N$_4$ MLs have been represented visually in Fig. 1a–c. The values of d_1, d_2, d_3, and $d_{M–N}$ outlined in Table 1 have been annotated in Fig. 1c. For example, d_1 presents the distance from the top N atom to the bottom N atom.

3.2. Electronic and magnetic properties of MSi$_2$N$_4$

Initially, our investigation is focused on the electromagnetic characteristics of a pcell. Each MSi$_2$N$_4$ pcell is composed of one M atom, two Si atoms, and four N atoms, each demonstrating spin charge densities as delineated in Fig. S2a–d (ESI†). The magnetic moments (MMs) attributed to each M atom equate to 2.56 (M = Cr), 3.31 (Mn), 3.84 (Fe), and 2.51 (Co) μ$_B$, in contrast to the MMs of silicon and nitrogen atoms, which approach 0 μ$_B$. The band structures and partial densities of states (PDOSs) of MSi$_2$N$_4$ have been computed and presented in Fig. S3a–d (ESI†), indicating that CrSi$_2$N$_4$ and CoSi$_2$N$_4$ MLs operating with the pcell are HMs, while MnSi$_2$N$_4$ and FeSi$_2$N$_4$ MLs function as semiconductors. Besides, the band structures with the SOC with the magnetic axis along [001] are also calculated, considering the existence of M in the MSi$_2$N$_4$ MLs. The calculation results are shown in Fig. 2a–d. For CrSi$_2$N$_4$, MnSi$_2$N$_4$ and FeSi$_2$N$_4$ MLs, the bands cross the Fermi-level, and thus they are metals. More specifically, the MnSi$_2$N$_4$ ML is a metal based on the SOC calculation results, while it is a semiconductor based on the band structures without the SOC. So, it is different between the band structures without the SOC and those with the SOC. For the CoSi$_2$N$_4$ ML, its VBM is located at the Γ point, while its CBM is located at the F point, as shown in Fig. 2d. Therefore, the CoSi$_2$N$_4$ ML is a semiconductor with an indirect band gap of 0.370 eV. Comprehensive data regarding the electromagnetic properties of MSi$_2$N$_4$ MLs can be found in the ESI.†
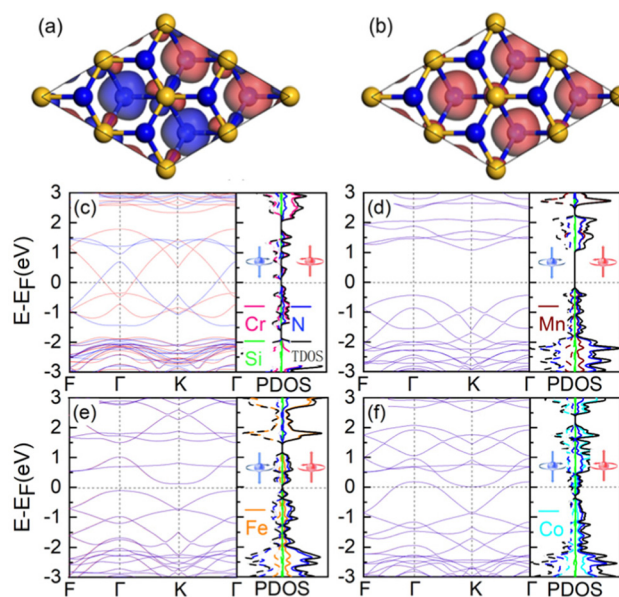
Subsequently, supercells of MSi$_2$N$_4$ MLs were studied to authenticate the ground states of the MSi$_2$N$_4$ compounds. Analysis of the magnetic properties of M atoms was conducted to discern the magnetic order, as displayed in Fig. 3a–c. Each M atom contributes 2.51 (Cr), 3.31 (Mn), 3.72 (Fe), and 2.55 (Co) μ$_B$ MM, with four M atoms present in a supercell. The FM order in the supercell yields 8.00 (CrSi$_2$N$_4$), 12.00 (MnSi$_2$N$_4$), 16.00 (FeSi$_2$N$_4$), and 11.35 (CoSi$_2$N$_4$) μ$_B$ MM, suggesting that the MM of MSi$_2$N$_4$ is principally contributed by M atoms, as demonstrated in Table 2. In addition to the FM order, the AFM configuration was also examined. For the AFM orders of the MSi$_2$N$_4$ MLs, two M atoms contribute positive MMs of 2.173, 3.194, 3.640, and 2.536 μ$_B$, while the other two M atoms contribute an equal and opposite MM, leading to a total MM of 0.0 μ$_B$ for all considered MSi$_2$N$_4$ MLs. Fig. 3a–c shows the spin charge densities of MSi$_2$N$_4$ for both FM and AFM orders. We define $\Delta E_{FM–AFM}$ as follows: $\Delta E_{FM-AFM} = E_{FM} - E_{AFM}$, which presents the energy differences between FM and AFM orders of MSi$_2$N$_4$ MLs. The energies of AFM orders of MSi$_2$N$_4$ MLs (E_{AFM})

Table 2 MM (μ$_B$) and the energy differences $\Delta E_{FM–AFM}$ (meV) of MSi$_2$N$_4$ MLs between FM and AFM orders. MM/M in the table represents the moment contributed by M atoms

System	ΔE_{FM-AFM}	MM		MM/M	
		FM	AFM	FM	AFM
CrSi$_2$N$_4$	438	8.00	0	2.51	±2.17
MnSi$_2$N$_4$	1235	12.00	0	3.31	±3.19
FeSi$_2$N$_4$	547	16.00	0	3.72	±3.64
CoSi$_2$N$_4$	138	11.35	0	2.55	±2.54

4210 | *Phys. Chem. Chem. Phys.*, 2024, **26**, 4208–4217

This journal is © the Owner Societies 2024

are set as 0 eV. The result shows that the energies of the FM orders E_{FM} are the highest among all calculated magnetic orders of the MSi_2N_4 MLs. ΔE_{FM-AFM} is shown in Table 2.

To comprehend why MSi_2N_4 MLs exhibit an AFM orientation, we delved into the underlying mechanism. Each M atom within the MSi_2N_4 MLs is surrounded by six N ligands. The N–Cr–N bond angles are precisely $69.898°$, $90.440°$, and $131.615°$, while the N–Mn–N bond angles are $69.539°$, $90.703°$, and $131.498°$. In the case of the $FeSi_2N_4$ ML, the N-Fe–N angles are $69.539°$, $90.702°$, and $131.498°$. For Co, the N–Co–N bond angles are $70.113°$, $90.294°$, and 131.679, respectively. Analysis of the Integrated Density of States (IDOS) of d-electrons suggested that M atoms contained between 4 and 7 electrons within d-orbitals. The presence of these electrons led to a direct exchange interaction that resulted in AFM coupling. Concurrently, the FM coupling was seen to arise from super-exchange interaction, in line with the Goodenough–Kanamori–Anderson rule[51-53] as controlled by the superexchange theorem. These two distinct exchange interactions were observed, with the direct exchange interaction between the M atoms playing a decisive role in defining the ground state, as depicted in Fig. S9a (ESI†). This implies that the direct exchange interaction among the M atoms proved stronger than the superexchange interaction, as illustrated in Fig. S9a and b (ESI†). Consequent to this analysis, MSi_2N_4 demonstrates an AFM ground state, in contrast to $MoSi_2N_4$. The MSi_2N_4 MLs with AFM orders were identified as either spin-unpolarized metals ($CrSi_2N_4$ and $CoSi_2N_4$) or semiconductors ($MnSi_2N_4$ and $FeSi_2N_4$), with respective energy gaps of 1.539 and 0.234 eV, as illustrated in Fig. 3d–g. Additional data on the magnetic and electronic properties of the MSi_2N_4 MLs are provided in Fig. S10 in the ESI.†

3.3. Electronic and magnetic properties of carrier-doped MSi_2N_4

Carrier-doped 2D materials have been realized by several methods,[54-57] such as self-doping caused by intrinsic defects,[58] bulk doping induced by the substrate,[59] spontaneous polarization associated with the substrate,[60] and so on.[61] The doping value is up to 10^{14}–10^{15} e cm^{-2} in some experimental studies[54-56] or theoretical research,[62-65] and so the chosen doping values in this work are reasonable. Additionally, carrier doping methodologies[40,66] have been frequently employed to modulate the performance characteristics of 2D materials. Hence, further investigations are warranted to scrutinize the effects of carrier doping on the magnetic and electronic properties of MSi_2N_4 MLs.

Our calculated findings indicate that charge doping exerts an influence on the properties of these MLs. Notably, carrier doping within MSi_2N_4 MLs can instigate a magnetic phase transition due to alterations in the number and structure of MSi_2N_4 valence electrons. These modifications have implications for the energy of each magnetic configuration, in compliance with the Goodenough–Kanamori–Anderson rule. Furthermore, carrier doping can initiate an electronic phase transition, effectively converting MSi_2N_4 MLs from semiconductors to HMs. Recognizing the potential for magnetic

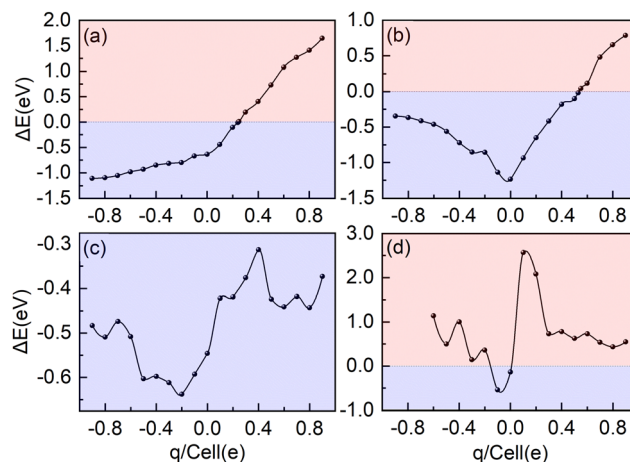**Fig. 4** Electron and hole doping of MSi_2N_4 MLs. ΔE values of (a) $CrSi_2N_4$, (b) $MnSi_2N_4$, (c) $FeSi_2N_4$, and (d) $CoSi_2N_4$ change with doped charges. The q in this figure presents the number of doped charges.

configuration regulation of MSi_2N_4 is vital, given the promising future of 2D FM materials in various applications such as integrated chips, spintronic devices, magnetic storage, and quantum information technology.[67] The charge doping could cause magnetic phase transformation from AFM to FM orders in MSi_2N_4. The energy differences between AFM and FM orders (ΔE) are defined as $\Delta E = E_{AFM} - E_{FM}$, where E_{AFM} means the energy of MSi_2N_4 with AFM order, while E_{FM} means the energy of MSi_2N_4 with FM order. The relation between ΔE and doped charges is shown in Fig. 4a–d. When -0.3 e per pcell (-0.0409 e Å^{-2}) charges are injected in the pcell of the $CrSi_2N_4$ ML, the ΔE is -0.816 eV. As more negative charges are introduced, the ΔE values are decreased to -0.982 eV (-0.6 e per pcell) and -1.110 eV (-0.9 e per pcell), respectively. When the holes (positive charges) are doped, the ΔE values are further increased to -0.442 eV ($+0.1$ e per pcell), 0.194 eV ($+0.3$ e per pcell), 1.078 eV ($+0.6$ e per pcell), and 1.646 eV ($+0.9$ e per pcell), respectively. The magnetic phase transition is observed in the $CrSi_2N_4$ ML when $+0.25$ e per pcell holes are doped, as shown in Fig. 4a. ΔE increases as more positive charges or fewer negative charges are doped. This means that the superexchange interaction is strengthened and the direct exchange interaction is weakened. Following the investigation of $CrSi_2N_4$ MLs, the magnetic properties of doped $MnSi_2N_4$ MLs are explored. The total energy difference (ΔE) of $MnSi_2N_4$ initially diminishes and subsequently escalates, as demonstrated in Fig. 4b. The nadir of ΔE is observed when $MnSi_2N_4$ MLs are in their undoped state, with a minimum value of -1.235 eV. Notably, a magnetic phase transition is evident in $MnSi_2N_4$ MLs upon the introduction of $+0.54$ e per pcell ($+0.0731$ e Å^{-2}) holes, as illustrated in Fig. 4b. The ΔE plots for both $FeSi_2N_4$ and $MnSi_2N_4$ MLs exhibit a V-shaped pattern, as evidenced in Fig. 4b and c. A persistent AFM order characterizes $FeSi_2N_4$, whereas $CoSi_2N_4$, upon carrier doping, predominantly exhibits an FM order, as shown in Fig. 4d.

The foregoing discussion reveals that carrier doping can influence the magnetic characteristics of MSi_2N_4 MLs. Additionally, it appears that carrier doping also mediates changes in
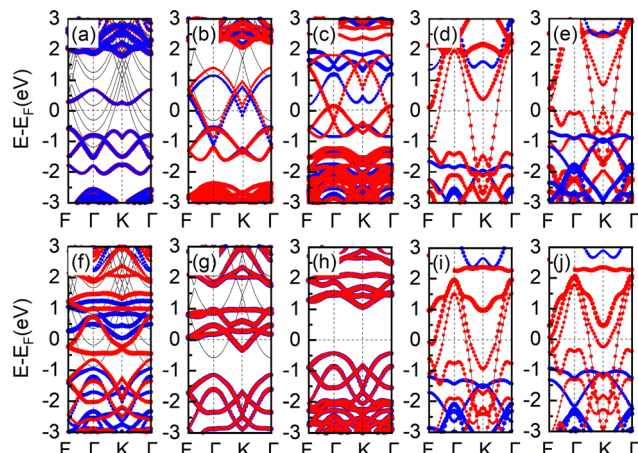
Fig. 5 Band structures of the electron or hole doped CrSi$_2$N$_4$ and MnSi$_2$N$_4$ MLs, calculated using HSE06 functional. The band structures of CrSi$_2$N$_4$ are doped with (a) −0.8, (b) −0.3, (c) 0.2, (d) 0.5, and (e) +0.8 e per pcell. MnSi$_2$N$_4$ is doped with (f) −0.6, (g) −0.3, (h) 0, (i) 0.6, and (j) 0.9 e, respectively. The red and blue lines represent spin-α and spin-β electrons, respectively.

Fig. 6 Information about the MAE of CrSi$_2$N$_4$. (a) Relationship between ΔE_0 and (θ,ϕ) is shown in a stereogram. (b) ΔE_0 of CrSi$_2$N$_4$ with different doped charges varies as elevation changes. The black, red, yellow, green, cyan, blue and purple dotted lines represent ΔE_0 of CrSi$_2$N$_4$ with doped charges of +0.3, +0.4, +0.5, +0.6, +0.7, +0.8, and +0.9 e per pcell holes, respectively. (c) Red arrows represent the direction of EA of MnSi$_2$N$_4$. (d) Relation between ΔE_0 of CrSi$_2$N$_4$ and azimuthal. The black, red, yellow, green, cyan, blue and purple dotted lines represent ΔE_0 of CrSi$_2$N$_4$ with doped charges of +0.3, +0.4, +0.5, +0.6, +0.7, +0.8, and +0.9 e per pcell, respectively.

electronic properties. As illustrated in Fig. 5, CrSi$_2$N$_4$ in its undoped state behaves as a metal, whereas undoped MnSi$_2$N$_4$ exhibits semiconductor characteristics. The metallic nature of CrSi$_2$N$_4$ persists with the introduction of −0.8 or −0.3 e per pcell electrons. However, with the addition of +0.2 e per pcell holes, the CrSi$_2$N$_4$ ML transforms into an HM, as delineated in Fig. 5c. This shift is noteworthy as it occurs upon the introduction of +0.2 e per pcell holes, suggesting a lower threshold for the modulation of electronic properties compared to magnetic transitions. As Fig. 5c–e indicate, the states proximate to the Fermi level in HMs are primarily attributed to spin-α electrons. The transition of CrSi$_2$N$_4$ from the semiconductor to HM is attributable to the repositioning of some electrons initially residing at the Fermi level, which are "pumped" out of the valence band maximum (VBM) of CrSi$_2$N$_4$ when positive charges are incorporated. This carrier doping modifies the Fermi surface, thereby triggering the transition. With regard to MnSi$_2$N$_4$, doping with −0.6 or −0.3 e per pcell charges imparts metallic characteristics, whereas in its undoped state, MnSi$_2$N$_4$ behaves as a semiconductor. The introduction of +0.6 or +0.9 e per pcell electrons induces a shift to the HM phase, as presented in Fig. 5f and g. Here, as in CrSi$_2$N$_4$, the states at the MnSi$_2$N$_4$ ML's Fermi level in the HM phase are predominantly due to spin-α electrons. Moreover, the HM phase persists when charges are introduced in the CoSi$_2$N$_4$ ML, with additional details provided in the Supporting Information (Fig S11, ESI†).

3.4. Magnetocrystalline anisotropy

The MAE is normally defined as the difference in total energy for moment alignment along an EA and a hard axis.[35,68] The elevation of the magnetic axis is defined as θ and the azimuth of the magnetic axis is defined as ϕ. The relation between the
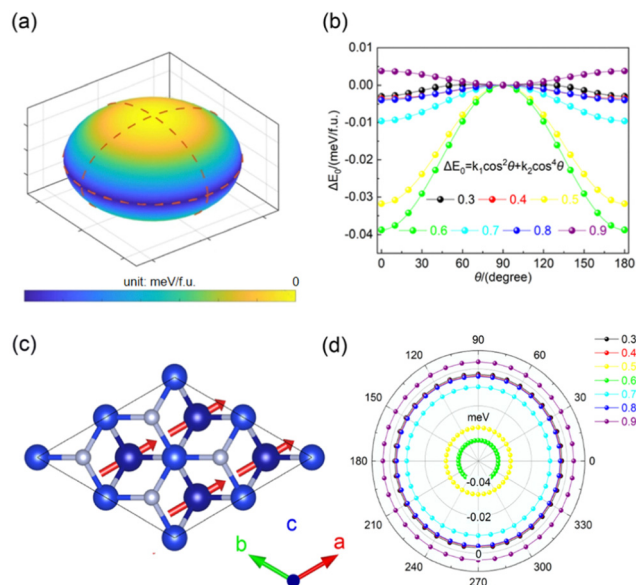
energies of the systems with high symmetry and (θ, ϕ) is as follows:[69]

$$\Delta E_0 = K_1 \cos^2\theta + K_2 \cos^4\theta + K_3 \cos 3\phi = E - E_{[001]} \tag{1}$$

In the above equation, E is the energy in a certain elevation and azimuth (θ,ϕ). $E_{[001]}$ represents the energy with the EA along the [001] direction. Similarly, $E_{[100]}$ and $E_{[010]}$ could be defined. K_1 and K_2 are the quadratic and quartic contributions to the MAE in eqn (1), respectively. The relation between ΔE_0 and (θ,ϕ) is shown in Fig. 6a. Previous literature[70] indicates that ΔE_0 and ϕ are independent. Besides, the conclusion could be drawn from the symmetry of the MSi$_2$N$_4$ MLs that each of the MSi$_2$N$_4$ MLs has a D_{3h} point group.[58] As a result, K_3 is equal to 0. Therefore, eqn (1) is corrected into the following equation:

$$\Delta E = K_1\cos^2\theta + K_2\cos^4\theta \tag{2}$$

For the MnSi$_2$N$_4$ ML, when $E = E_{001}$ and $\theta = \pi/2$, ΔE_0 reaches the maximum value (0 meV, taken as the reference energy). However, it reaches the minimum value when $\theta = 0$. The EA tends to be IMA (in-plane magnetic anisotropy, along the [100] direction). The relation between ΔE_0 and θ is revealed in Fig. 7a. In calculation, U_{eff} is set as 4.6 eV. The relation between the ΔE_0 (unit: meV) of the different charge doped MnSi$_2$N$_4$ ML and θ is as follows: $\Delta E_0 = -0.209\cos^2\theta$(+0.6 e),
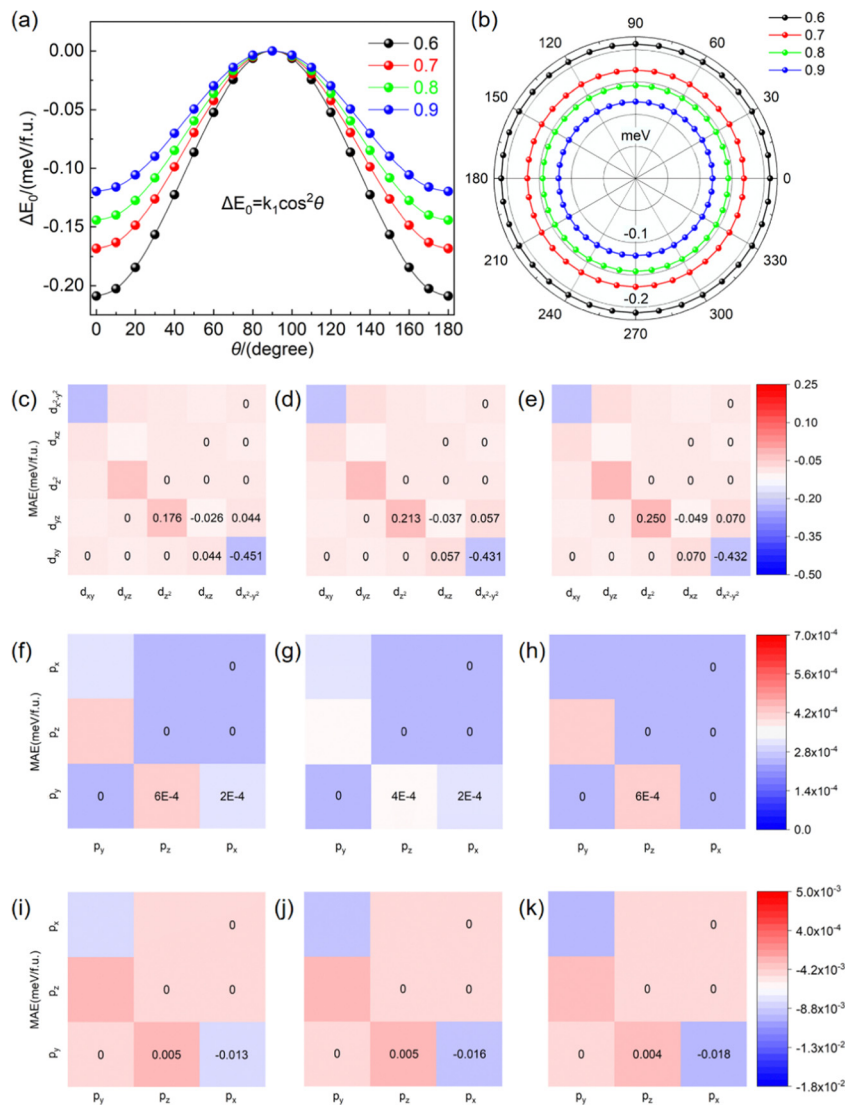
Fig. 7 (a) ΔE_0 of the doped MnSi$_2$N$_4$ ML varies as elevation changes. The black, red, green and blue dotted lines represent the ΔE_0 of MnSi$_2$N$_4$ with +0.6, +0.7, +0.8, and +0.9 e per pcell doped charges varying as elevation changes. (b) ΔE_0 values of MnSi$_2$N$_4$ with different doped charges vary as azimuthal changes. The black, red, green and blue dotted lines represent the ΔE_0 of MnSi$_2$N$_4$ with +0.6, +0.7, +0.8, and +0.9 e per pcell doped charges varying as azimuthal changes. Orbital-resolved MAE of the MnSi$_2$N$_4$ ML with doped charges of (c) and (f) and (i) +0.6, (d) and (g) and (j) +0.8, and (e) and (h) and (k) +1.0 e per pcell, respectively. The orbital-resolved MAEs contributed by (c) and (d) and (e) Mn, (f) and (g) and (h) Si, and (i) and (j) and (k) N atoms are shown in this figure, respectively.

$\Delta E_0 = -0.168\cos^2\theta(+0.7\ e)$, $\Delta E_0 = -0.144\cos^2\theta(+0.8\ e)$, and $\Delta E_0 = -0.120\cos^2\theta(+0.9\ e)$. $E_{[100]}$ and $E_{[001]}$ are used to represent the energies of the system whose θ values of the magnetic axis are 0 and 90 degrees, respectively. Then MAE could be presented as the following equation:

$$\text{MAE} = E_{[100]} - E_{[001]} \tag{3}$$

When MAE is negative, the direction of the EA tends to be in the plane, and it is called as IMA. By the way, when the EA prefers to be perpendicular to the plane, it is called perpendicular magnetic anisotropy (PMA). MnSi$_2$N$_4$ is a 2D material, and it is expected that the MnSi$_2$N$_4$ ML has a considerable MAE compared with a three-dimensional material. The calculation results reveal that the MAEs of the MnSi$_2$N$_4$ ML are -0.209

(+0.6 e per pcell), -0.168 (+0.7 e per pcell), -0.144 (+0.8 e per pcell), and -0.120 meV (+0.9 e per pcell), respectively. Negative MAE indicates that MnSi$_2$N$_4$ prefers IMA, as shown in Fig. 6c. The MAE of MnSi$_2$N$_4$ decreases with the increase of doped charges, as shown in Fig. 7a and b. CrSi$_2$N$_4$ is similar to that of the MnSi$_2$N$_4$ ML. The U_{eff} is also set as 4.0 eV for the MnSi$_2$N$_4$ ML. The relation between ΔE_0 (unit: μeV) and θ is revealed in Fig. 6b. Besides, the relation between the ΔE_0 of the CrSi$_2$N$_4$ ML with different carrier doping and θ is as follows:

$$\Delta E_0 = -7.45\cos^2\theta + 4.52\cos^4\theta(+0.3\ e) \tag{4}$$

$$\Delta E_0 = -2.61\cos^2\theta - 0.95\cos^4\theta(+0.4\ e) \tag{5}$$

$$\Delta E_0 = -31.77\cos^2\theta(+0.5\ e) \tag{6}$$

This journal is © the Owner Societies 2024

Phys. Chem. Chem. Phys., 2024, **26**, 4208–4217 | **4213**

$$\Delta E_0 = -38.76\cos^2\theta\,(+0.6\ \text{e}) \tag{7}$$

$$\Delta E_0 = -9.59\cos^2\theta\,(+0.7\ \text{e}) \tag{8}$$

$$\Delta E_0 = -3.93\cos^2\theta\,(+0.8\ \text{e}) \tag{9}$$

$$\Delta E_0 = 3.77\cos^2\theta\,(+0.9\ \text{e}) \tag{10}$$

The MAEs of the $CrSi_2N_4$ ML are -2.93 ($+0.3$ e per pcell), -3.56 ($+0.4$ e per pcell), -31.78 ($+0.5$ e per pcell), -38.77 ($+0.6$ e per pcell), -9.59 ($+0.7$ e per pcell), -3.93 ($+0.8$ e per pcell), and 3.76 ($+0.9$ e per pcell) μeV, respectively, as shown in Fig. 6d. MAEs of $CrSi_2N_4$ decrease first and then increase. Interestingly, when $+0.9$ e per pcell electrons are introduced, the negative MAE value substitutes for the positive one, which means that the EA of the $CrSi_2N_4$ ML has changed from [100] to [001] directions. Accordingly, there is a switch for $CrSi_2N_4$ from IMA to PMA.

In order to clarify the switch of EA, it is necessary to determine the contribution of each atomic orbital to the MAE of $CrSi_2N_4$ and $MnSi_2N_4$. Besides, explaining the relation between MAEs (MAEs of $CrSi_2N_4$ and $MnSi_2N_4$) and doped charges is urgent. To accomplish the above objectives, tight binding and second-order perturbation theory are used to calculate the MAE.[59] According to the canonical formula,[71] each atom's contribution to MAE can be calculated by using the following formula:

$$\text{MAE}_i = \left[\int E_f (E - E_F)[n_i^{[100]}(E) - n_i^{[001]}(E)] \right] \tag{11}$$

where MAE_i represents the MAE contributed by atom i and $n_i^{[100]}$ and $n_i^{[001]}$ mean the density of state in [100] and [001] directions, respectively. Given the symmetry of MSi_2N_4 MLs (D_{3h} group), $E_{[010]}$ is equal to $E_{[100]}$.[33] The following formula is used to calculate the total MAE:

$$\text{MAE}_{\text{tot}} = \sum_i \text{MAE}_i \tag{12}$$

where MAE_{tot} is the sum of MAE_i. Given the second-order perturbation theory,[72] MAE can be calculated using the following equation:

$$\begin{aligned}\Delta E^{--} &= E_x^{--} - E_z^{--} \\ &= \xi^2 \sum_{o^+, u^-} \left(|\langle o^-|L_z|u^-\rangle|^2 - |\langle o^-|L_x|u^-\rangle|^2 \right) / (E_u^- - E_o^-)\end{aligned} \tag{13}$$

$$\begin{aligned}\Delta E^{-+} &= E_x^{+-} - E_z^{+-} \\ &= \xi^2 \sum_{o^+, u^-} \left(|\langle o^+|L_z|u^-\rangle|^2 - |\langle o^+|L_x|u^-\rangle|^2 \right) / (E_u^- - E_o^-)\end{aligned} \tag{14}$$

where $+$ and $-$ mean spin-α and spin-β states and ξ, L_x and L_z represent the SOC constant and angular momentum operators in [100] and [001] directions, respectively. u and o represent unoccupied and occupied states, respectively. E_u and E_o represent the energies of occupied and unoccupied states, respectively. MAE is primarily composed of spin orbit matrix element and energy difference. According to eqn (4), MAE is related to the density of states near the Fermi-level. The matrix element differences $\langle o^-|L_z|u^-\rangle|^2 - |\langle o^-|L_x|u^-\rangle|^2$ and

Table 3 Matrix differences of d orbitals along [001] and [100] directions in eqn (6) and (7)

u^-	o^+					o^-				
	d_{xy}	d_{yz}	d_{z^2}	d_{xz}	$d_{x^2-y^2}$	d_{xy}	d_{yz}	d_{z^2}	d_{xz}	$d_{x^2-y^2}$
d_{xy}	0	0	0	1	-4	0	0	0	-1	4
d_{yz}	0	0	3	-1	1	0	0	-3	1	-1
d_{z^2}	0	3	0	0	0	0	-3	0	0	0
d_{xz}	1	-1	0	0	0	-1	1	0	0	0
$d_{x^2-y^2}$	-4	1	0	0	0	4	-1	0	0	0

$\langle o^+|L_z|u^-\rangle|^2 - |\langle o^+|L_x|u^-\rangle|^2$ of p and d orbitals are calculated and are shown in Table 3 and Table 4.

To explain the change in MAE with doped charges, atomic orbital resolved MAE is researched, and the corresponding results are shown in Fig. 7c–k and Fig. 8a–i, respectively. The MAE of $CrSi_2N_4$ is relatively low. Each atom's contribution to the MAE is shown in Table S1 (ESI†). The hybridization between the d orbitals of Cr is also investigated. It could be concluded that the hybridization between the d_{z^2} and d_{yz} of Cr atoms contributes positively to MAE (corresponds to a matrix difference of 3 for the d-orbitals) from 0.040 ($+0.6$ e per pcell) to 0.051 ($+0.9$ e per pcell) meV. The hybridization between the $d_{x^2-y^2}$ and d_{xy} of Cr atoms makes negative contribution to MAE (corresponds to a matrix difference of -4 for the d-orbitals of Cr atoms) from -0.060 ($+0.6$ e per pcell) to -0.033 ($+0.9$ e per pcell) meV. More information about the hybridization between the d orbitals of Cr could be found in Fig. 8a–i. According to the above results, we can conclude that the negative contribution (to MAE) of the hybridization between the $d_{x^2-y^2}$ and d_{xy} of Cr atoms decreases with the doped charges. Besides, the positive contribution (to MAE) of the hybridization between the d_{z^2} and d_{yz} of Cr atoms increases with the doped charges. These could explain the fact that the MAE's sign reverses, which means the transformation of the EA.

3.5. Dynamical and thermal stability

The phonon dispersion curve and the PHDOS are calculated, as shown in Fig. 9a–d. The results show that there is no imaginary phonon mode, and thus the dynamic stability of MSi_2N_4 is predicted. The highest vibrational frequencies contributed by M are 11.97 (Cr), 6.53 (Mn), 5.28 (Fe) and 5.23 (Co) THz, respectively, which decrease with the increasing atomic number. In addition, the PHDOS is mainly contributed by the M atom for the low frequency ($0 < \varepsilon < 10$ THz), while it is mainly contributed by N and Si atoms for the high frequency ($\varepsilon > 10$ THz). This difference is due to the different atomic weights of Si, N and M atoms. Specifically, the M atoms (atomic weights: 52.00, 54.94,

Table 4 Matrix differences of p orbitals along [001] and [100] directions in eqn (6) and (7)

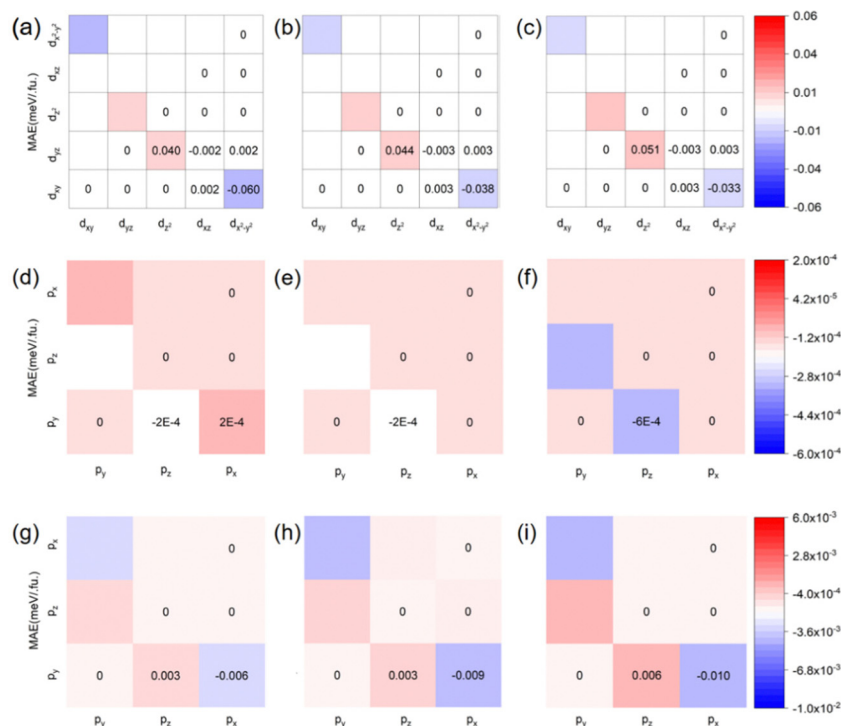| u^-	o^+			o^-		
	p_y	p_z	p_x	p_y	p_z	p_x
p_y	0	1	-1	0	-1	1
p_z	1	0	0	-1	0	0
p_x	-1	0	0	1	0	0

Fig. 8 Orbital-resolved MAE of the CrSi$_2$N$_4$ ML with doped charges of (a) and (d) and (g) +0.6, (b) and (e) and (h) +0.7, and (c) and (f) and (i) +0.9 e per pcell, respectively. The orbital-resolved MAEs contributed by (a) and (b) and (c) Cr, (d) and (e) and (f) Si, and (g) and (h) and (i) N atoms are shown in this figure, respectively.

55.85, and 58.93) are heavier than Si (atomic weight: 28.09) and N atoms (atomic weight: 14.01). Thus, the high frequency phonons are mainly contributed by the silicon and nitrogen atoms, while the low frequency phonons are mainly contributed by the M atoms, as shown in Fig. 9a–d. M atoms contribute thermal conductivity mainly at low temperatures with the low-frequency phonons. However, thermal conductivity is mainly contributed by silicon and nitrogen atoms at high temperatures with the high-frequency phonons. Since the MSi$_2$N$_4$ MLs are composed of the same non-metallic atoms, and these non-metallic atoms are lighter than the M and Mo atoms, the maximum vibrational frequency of MSi$_2$N$_4$ is close to that of MoSi$_2$N$_4$.[73]

To predict the thermal stability of the MSi$_2$N$_4$ family, the widely used AIMD simulation, which is applied for studying the stability of materials, is performed at 300 K. The result shows that the total energies of MSi$_2$N$_4$ fluctuated around −219.65 (Cr), −216.77 (Mn), −207.41 (Fe), and −198.58 eV (Co) at 300 K, as shown in Fig. 9e–h. The total energies of MSi$_2$N$_4$ increase with the atomic number. The phase transition occurs in the CoSi$_2$N$_4$ ML, and the energy of the CoSi$_2$N$_4$ ML decreases during this phase transition. More information about the dynamical and thermal stability of MSi$_2$N$_4$ is shown in Fig S12 in the ESI.†

4. Conclusion

In summary, we employed DFT calculations to investigate the structural, electronic, and magnetic properties of MSi$_2$N$_4$ MLs. We discovered that intrinsic MSi$_2$N$_4$ MLs exhibit either metallic or semiconducting behavior, coupled with AFM orders. We further investigated the impact of carrier doping on these

systems. Our results indicate that upon doping with +0.25 e per pcell (CrSi$_2$N$_4$)/+0.54 e per pcell (MnSi$_2$N$_4$) or more positive carriers, the magnetic orders of both CrSi$_2$N$_4$ and MnSi$_2$N$_4$ MLs transform into FM states. Moreover, charge doping appears to be a viable strategy to modulate the electronic properties of these MLs. Indeed, CrSi$_2$N$_4$ and MnSi$_2$N$_4$ can transform from their initial states as metals or semiconductors into HMs upon the introduction of +0.5 e per pcell/+0.6 e per pcell charges, respectively. Further injection of positive charges results in an initial increase followed by a decrease in the MAE of CrSi$_2$N$_4$ beyond +0.6 e per pcell charge doping. Interestingly, carrier doping of +0.9 e per pcell causes a switch in the EA direction from [100] to [001] in the CrSi$_2$N$_4$ ML. This phenomenon is attributable to the reduced negative hybridization contribution between the d$_{x^2-y^2}$ and d$_{xy}$ orbitals of Cr atoms and the increased positive hybridization contribution between the d$_{z^2}$ and d$_{yz}$ orbitals of Cr atoms, resulting from the introduced additional positive charges. On the other hand, the MAE of MnSi$_2$N$_4$ diminishes with charge doping, which can be ascribed to the decreased negative hybridization contribution between the d$_{xy}$ and d$_{x^2-y^2}$ of Mn atoms and the increased positive hybridization contribution between the d$_{z^2}$ and d$_{yz}$, d$_{xy}$ and d$_{xz}$ of Mn atoms. Our findings highlight the excellent tunable electromagnetic properties of MSi$_2$N$_4$ MLs. We are hopeful that this study will serve as a springboard for further theoretical and experimental investigations in the burgeoning field of 2D magnetic materials.

Conflicts of interest

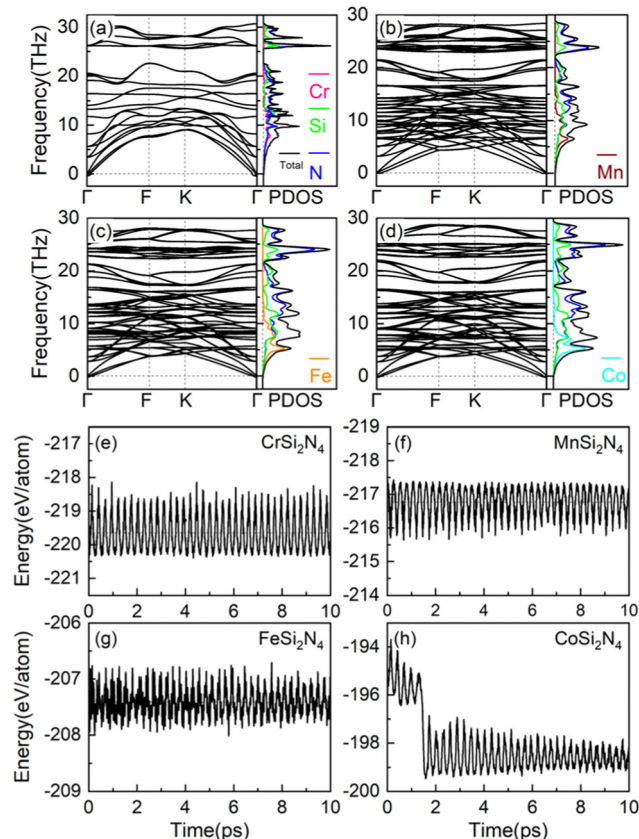The authors declare no competing financial interest.

Fig. 9 (a)–(d) Phonon spectrum and PHDOS of (a) $CrSi_2N_4$, (b) $MnSi_2N_4$, (c) $FeSi_2N_4$, and (d) $CoSi_2N_4$ MLs. The green, blue, pink, wine red, orange, cyan lines represent the projected phonon DOS of Si, N, Cr, Mn, Fe, and Co atoms, respectively. (e)–(h) AIMD of evaluation of energies at the PBE + U level for 10 ps at 300 K. The total energies of (e) $CrSi_2N_4$, (f) $MnSi_2N_4$, (g) $FeSi_2N_4$, and (h) $CoSi_2N_4$ are shown in (e) and (h), respectively.

Acknowledgements

References

1 K. S. Novoselov, A. K. Geim, S. V. Morozov, D. Jiang, Y. Zhang, S. V. Dubonos, I. V. Grigorieva and A. A. Firsov, *Science*, 2004, **306**, 666–669.

2 T. Y. Kim, C. H. Park and N. Marzari, *Nano Lett.*, 2016, **16**, 2439–2443.

3 D. Cohen-Tanugi and J. C. Grossman, *Nano Lett.*, 2014, **14**, 6171–6178.

4 A. R. Muniz, A. S. Machado and D. Maroudas, *Carbon*, 2015, **81**, 663–677.

5 F. I. Alzakia, B. S. Tang, S. J. Pennycook and S. C. Tan, *Mater. Horiz.*, 2020, **7**, 3325–3338.

6 Y. L. An, Y. Tian, C. L. Wei, Y. C. Zhang, S. L. Xiong, J. K. Feng and Y. T. Qian, *Energy Storage Mater.*, 2020, **32**, 115–150.

7 N. Ashraf, M. I. Khan, A. Majid, M. Rafique and M. B. Tahir, *Chinese J. Phys.*, 2020, **66**, 246–257.

8 Y. Zhou, J. Zhang, E. H. Song, J. H. Lin, J. D. Zhou, K. Suenaga, W. Zhou, Z. Liu, J. J. Liu, J. Lou and H. J. Fan, *Nat. Commun.*, 2020, **11**, 2253.

9 N. D. Mermin and H. Wagner, *Phys. Rev. Lett.*, 1966, **17**, 1133–1136.

10 B. Huang, G. Clark, E. Navarro-Moratalla, D. R. Klein, R. Cheng, K. L. Seyler, D. Zhong, E. Schmidgall, M. A. McGuire, D. H. Cobden, W. Yao, D. Xiao, P. Jarillo-Herrero and X. D. Xu, *Nature*, 2017, **546**, 270–273.

11 J. Seo, D. Y. Kim, E. S. An, K. Kim, G. Y. Kim, S. Y. Hwang, D. W. Kim, B. G. Jang, H. Kim, G. Eom, S. Y. Seo, R. Stania, M. Muntwiler, J. Lee, K. Watanabe, T. Taniguchi, Y. J. Jo, J. Lee, B. I. Min, M. H. Jo, H. W. Yeom, S. Y. Choi, J. H. Shim and J. S. Kim, *Sci. Adv.*, 2020, **6**, eaay8912.

12 B. Y. Zhou, Y. P. Wang, G. B. Osterhoudt, P. Lampen-Kelley, D. Mandrus, R. He, K. S. Burch and E. A. Henriksen, *J. Phys. Chem. Solids*, 2019, **128**, 291–295.

13 Z. W. Zhang, J. Z. Shang, C. Y. Jiang, A. Rasmita, W. B. Gao and T. Yu, *Nano Lett.*, 2019, **19**, 3138–3142.

14 M. Gibertini, M. Koperski, A. F. Morpurgo and K. S. Novoselov, *Nat. Nanotechnol.*, 2019, **14**, 408–419.

15 N. Z. Wang, H. B. Tang, M. Z. Shi, H. Zhang, W. Z. Zhuo, D. Y. Liu, F. B. Meng, L. K. Ma, J. J. Ying, L. J. Zou, Z. Sun and X. H. Chen, *J. Am. Chem. Soc.*, 2019, **141**, 17166–17173.

16 I. A. Verzhbitskiy, H. Kurebayashi, H. X. Cheng, J. Zhou, S. Khan, Y. P. Feng and G. Eda, *Nat. Electron.*, 2020, **3**, 460–465.

17 M. Bonilla, S. Kolekar, Y. J. Ma, H. C. Diaz, V. Kalappattil, R. Das, T. Eggers, H. R. Gutierrez, M. H. Phan and M. Batzill, *Nat. Nanotechnol.*, 2018, **13**, 289–293.

18 K. F. Mak, C. Lee, J. Hone, J. Shan and T. F. Heinz, *Phys. Rev. Lett.*, 2010, **105**, 136805.

19 K. S. Novoselov, D. Jiang, F. Schedin, T. J. Booth, V. V. Khotkevich, S. V. Morozov and A. K. Geim, *Proc. Natl. Acad. Sci. U. S. A.*, 2005, **102**, 10451–10453.

20 L. K. Li, Y. J. Yu, G. J. Ye, Q. Q. Ge, X. D. Ou, H. Wu, D. L. Feng, X. H. Chen and Y. B. Zhang, *Nat. Nanotechnol.*, 2014, **9**, 372–377.

21 X. Jiang, Q. X. Liu, J. P. Xing, N. S. Liu, Y. Guo, Z. F. Liu and J. J. Zhao, *Appl. Phys. Rev.*, 2021, **8**, 031305.

22 X. X. Li and J. L. Yang, *Nat. Sci. Rev.*, 2016, **3**, 365–381.

23 Y. L. Hong, Z. B. Liu, L. Wang, T. Y. Zhou, W. Ma, C. Xu, S. Feng, L. Chen, M. L. Chen, D. M. Sun, X. Q. Chen, H. M. Cheng and W. C. Ren, *Science*, 2020, **369**, 670–674.

24 A. K. Geim and K. S. Novoselov, *Nat. Mater.*, 2007, **6**, 183–191.

25 N. Lu, H. Y. Guo, L. Li, J. Dai, L. Wang, W. N. Mei, X. J. Wu and X. C. Zeng, *Nanoscale*, 2014, **6**, 2879–2886.

26 X. Chen, H. Yang, B. Wu, L. F. Wang, Q. Fu and Y. Q. Liu, *Adv. Mater.*, 2019, **31**, 1805582.

27 J. B. Smith, D. Hagaman and H. F. Ji, *Nanotechnology*, 2016, **27**, 215602.

28 M. Osada and T. Sasaki, *J. Mater. Chem.*, 2009, **19**, 2503–2511.

29 Q. Wang and D. O'Hare, *Chem. Rev.*, 2012, **112**, 4124–4155.

30 B. Mortazavi, B. Javvaji, F. Shojaei, T. Rabczuk, A. V. Shapeev and X. Y. Zhuang, *Nano Energy*, 2021, **82**, 105716.

31 K. S. Novoselov, A. Mishchenko, A. Carvalho and A. H. C. Neto, *Science*, 2016, **353**, 461.

32 H. Li, S. C. Ruan and Y. J. Zeng, *Adv. Mater.*, 2019, **31**, 1900065.

33 Z. Y. Guan and S. Ni, *J. Phys. Chem. C*, 2021, **125**, 16700–16710.

34 A. Avsar, A. Ciarrocchi, M. Pizzochero, D. Unuchek, O. V. Yazyev and A. Kis, *Nat. Nanotechnol.*, 2019, **14**, 674–678.

35 Z. Y. Guan and S. Ni, *ACS Appl. Mater. Interfaces*, 2020, **12**, 53067–53075.

36 C. Gong, L. Li, Z. Li, H. Ji, A. Stern, Y. Xia, T. Cao, W. Bao, C. Wang, Y. Wang, Z. Q. Qiu, R. J. Cava, S. G. Louie, J. Xia and X. Zhang, *Nature*, 2017, **546**, 265–269.

37 X. X. Zhao, P. Song, C. C. Wang, A. C. Riis-Jensen, W. Fu, Y. Deng, D. Y. Wan, L. X. Kang, S. C. Ning, J. D. Dan, T. Venkatesan, Z. Liu, W. Zhou, K. S. Thygesen, X. Luo, S. J. Pennycook and K. P. Loh, *Nature*, 2020, **581**, 171–177.

38 V. G. Pleshchev and N. V. Selezneva, *Phys. Solid State*, 2019, **61**, 339–344.

39 J. He and T. Frauenheim, *J. Phys. Chem. C*, 2020, **11**, 6219–6226.

40 N. N. Luo, C. Si and W. H. Duan, *Phys. Rev. B*, 2017, **95**, 205432.

41 R. Z. Xu, X. L. Zou, B. L. Liu and H. M. Cheng, *Mater. Today*, 2018, **21**, 391–418.

42 Y. C. Wang, J. A. Lv, L. Zhu and Y. M. Ma, *Phys. Rev. B: Condens. Matter Mater. Phys.*, 2010, **82**, 094116.

43 G. Kresse and J. Furthmuller, *Comput. Mater. Sci.*, 1996, **6**, 15–50.

44 J. P. Perdew, K. Burke and M. Ernzerhof, *Phys. Rev. Lett.*, 1996, **77**, 3865–3868.

45 J. Heyd, G. E. Scuseria and M. Ernzerhof, *J. Chem. Phys.*, 2003, **118**, 8207–8215.

46 J. Heyd, G. E. Scuseria and M. Ernzerhof, *J. Chem. Phys.*, 2006, **124**, 219906.

47 A. I. Liechtenstein, V. I. Anisimov and J. Zaanen, *Phys. Rev. B: Condens. Matter Mater. Phys.*, 1995, **52**, R5467–R5470.

48 A. Togo and I. Tanaka, *Scripta Mater.*, 2015, **108**, 1–5.

49 S. Nose, *J. Chem. Phys.*, 1984, **81**, 511–519.

50 B. X. Liu, H. L. Yao, L. Y. Wan, C. J. Liang, Y. S. Li, Z. H. Su and Y. S. Li, *ECS J. Solid State Sci. Technol.*, 2022, **11**, 073009.

51 P. W. Anderson, *Phys. Rev.*, 1950, **79**, 350–356.

52 J. B. Goodenough, *Phys. Rev.*, 1955, **100**, 564–573.

53 J. Kanamori, *J. Phys. Chem. Solids*, 1959, **10**, 87–98.

54 H. Yuan, H. Shimotani, A. Tsukazaki, A. Ohtomo, M. Kawasaki and Y. Iwasa, *Adv. Funct. Mater.*, 2009, **19**, 1046–1053.

55 T. Ciuk, W. Kaszub, K. Kosciewicz, A. Dobrowolski, J. Jagiello, A. Chamryga, J. Gaca, M. Wojcik, D. Czolak, B. Stanczyk, K. Przyborowska, R. Kozlowski, M. Kozubal, P. P. Michalowski, M. J. Szary and P. Kaminski, *Curr. Appl. Phys.*, 2021, **27**, 17–24.

56 A. S. Dhoot, C. Israel, X. Moya, N. D. Mathur and R. H. Friend, *Phys. Rev. Lett.*, 2009, **102**, 136402.

57 J. Sławińska, H. Aramberri, M. C. Muñoz and J. I. Cerdá, *Carbon*, 2015, **93**, 88–104.

58 Q. Liang, Q. Zhang, X. Zhao, M. Liu and A. T. S. Wee, *ACS Nano*, 2021, **15**, 2165–2181.

59 N. Liu, S. Zhou and J. Zhao, *Phys. Rev. Mater.*, 2020, **4**, 094003.

60 S. Wan, Y. Li, W. Li, X. Mao, W. Zhu and H. Zeng, *Nanoscale*, 2018, **10**, 14885–14892.

61 L. Wang, Z. Guo, Q. Lan, W. Song, Z. Zhong, K. Yang, T. Zhao, H. Huang, C. Zhang and W. Shi, *Micromachines*, 2023, **14**, 2125.

62 X. Li, X. Wu and J. Yang, *J. Am. Chem. Soc.*, 2014, **136**, 11065–11069.

63 W.-Q. Xie, Z.-W. Lu, C.-C. He, X.-B. Yang and Y.-J. Zhao, *J. Phys.: Condens. Matter*, 2021, **33**, 215803.

64 Y. Liang, X. Lv and T. Frauenheim, *Nanoscale*, 2022, **14**, 3261–3268.

65 H. Tan, G. Shan and G. Pacchioni, *Phys. Chem. Chem. Phys.*, 2021, **23**, 25500–25506.

66 Z. Y. Guan, W. Y. Wang, J. Huang, X. J. Wu, Q. X. Li and J. L. Yang, *J. Phys. Chem. C*, 2014, **118**, 28616–28624.

67 B. Peng, Z. Y. Chen, Y. Li, Z. Liu, D. F. Liang and L. J. Deng, *Iscience*, 2022, **25**, 103623.

68 Z. Y. Guan and S. Ni, *Nanoscale*, 2020, **12**, 22735–22742.

69 A. N. Bogdanov and I. E. Dragunov, *Low Temp. Phys.*, 1998, **24**, 852–857.

70 S. Q. Zhang, R. Z. Xu, W. H. Duan and X. L. Zou, *Adv. Funct. Mater.*, 2019, **29**, 1808380.

71 D. Z. Li, C. Barreteau, M. R. Castell, F. Silly and A. Smogunov, *Phys. Rev. B: Condens. Matter Mater. Phys.*, 2014, **90**, 205409.

72 D. S. Wang, R. Q. Wu and A. J. Freeman, *Phys. Rev. B: Condens. Matter Mater. Phys.*, 1993, **47**, 14932–14947.

73 J. H. Yu, J. Zhou, X. G. Wan and Q. F. Li, *New J. Phys.*, 2021, **23**, 033005.

This journal is © the Owner Societies 2024

Phys. Chem. Chem. Phys., 2024, **26**, 4208–4217 | **4217**